Rearrangement of Annular Rings of High Vorticity

Huiqun Wang
California Institute of Technology

1 Introduction

Flight level measurements suggest that hurricanes have low vorticity eyes surrounded by high vorticity eyewalls (Kossin and Schubert 2001). The rearrangement of such high vorticity annular rings is an important factor in hurricane dynamics. In this study, I use a barotropic nondivergent model to investigate the evolution of a set of high vorticity annular rings with fixed circulation and scales similar to hurricanes.

The initial radial profile of vorticity is given by

$$\zeta = \zeta_0 \begin{cases} 0, & 0 \le r \le r_1, \\ S\left((r_2 - r)/(r_2 - r_1)\right), & r_1 \le r \le r_2, \\ S\left((r - r_2)/(r_3 - r_2)\right), & r_2 \le r \le r_3, \\ 0, & r \ge r_3, \end{cases} \tag{1}$$

where $S(x) = 1 - 3x^2 + 2x^3$, r_2 is fixed at 60 km, $r_3 - r_1$ ranges from 4 km to 116 km with an increment of 4 km, and the constant ζ_0 is chosen so that all the rings have the same circulation for $r \ge r_3$. Sample initial vorticity and aximuthal wind profiles are shown in Fig. 1.

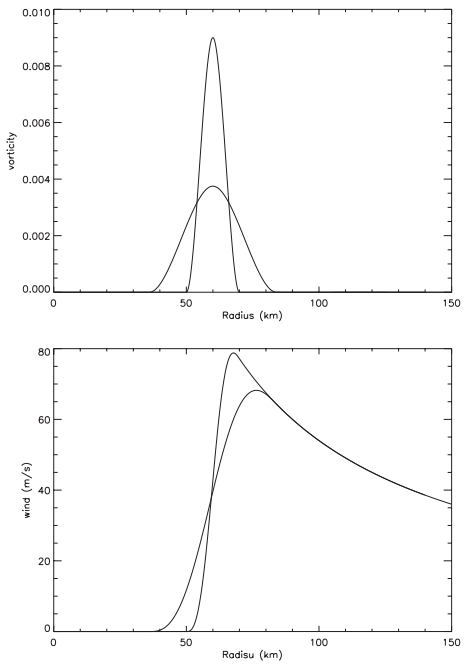

Figure 1: Sample radial profiles of the initial vorticity and tangential wind.

After introducing the numerical model, I describe the simulated evolution of representative narrow, wide, and very wide annular rings. I then compare the initial wavenumber with the published results of linear stability analysis, and investigate the history of the domain-averaged enstrophy for different rings. I apply the minimum enstrophy theory to predict the final states, and investigate the advantages and disadvantages of the theory. I also compare the results for these rings with two sets of skewed rings.

2 Numerical Model

An adaptive multigrid barotropic nondivergent model (Fulton 2001) was used to simulate the evolution of the annular rings. This model solves the modified barotropic vorticity equation in Mercator coordinates

$$\frac{\partial q}{\partial t} + m^2 \frac{\partial(\psi, q)}{\partial(x, y)} + \beta m \frac{\partial \psi}{\partial x} = \nu m^2 \left(\frac{\partial^2 q}{\partial x^2} + \frac{\partial^2 q}{\partial y^2} \right), \tag{2}$$

$$m^2 \left(\frac{\partial^2 \psi}{\partial x^2} + \frac{\partial^2 \psi}{\partial y^2} \right) - \gamma^2 \psi = q, \tag{3}$$

where $q = \zeta - \gamma^2 \psi$ is the potential vorticity anomaly, ζ is the relative vorticity, $f = 2\Omega \sin \phi$ is the Coriolis parameter, $\beta = df/ad\phi = 2\Omega a^{-1} \cos \phi$, $m = \cos \phi_0 / \cos \phi$ is the map factor, $\gamma^{-1} = \sqrt{gH}/f$ is the Rossby radius of deformation, ψ is the stream function, and ν is the constant viscosity.

In this study, I ran the model in the pure barotropic, f-plane mode by setting $\gamma = 0$, $m = 1$, and $\beta = 0$, so that the actual equations solved become

$$\frac{\partial \zeta}{\partial t} + \frac{\partial(\psi, \zeta)}{\partial(x, y)} = \nu \left(\frac{\partial^2 \zeta}{\partial x^2} + \frac{\partial^2 \zeta}{\partial y^2} \right), \tag{4}$$

$$\frac{\partial^2 \psi}{\partial x^2} + \frac{\partial^2 \psi}{\partial y^2} = \zeta. \tag{5}$$

Associated with this model are the kinetic energy and enstrophy equations

$$\frac{d\mathcal{E}}{dt} = -2\nu \mathcal{Z}, \tag{6}$$

$$\frac{d\mathcal{Z}}{dt} = -2\nu \mathcal{P}, \tag{7}$$

where $\mathcal{E} = \iint \frac{1}{2} \nabla\psi \cdot \nabla\psi \, dxdy$ is the energy, $\mathcal{Z} = \iint \frac{1}{2} \zeta^2 \, dxdy$ is the enstrophy, $\mathcal{P} = \iint \frac{1}{2} \nabla\zeta \cdot \nabla\zeta \, dxdy$ is the palinstrophy.

The numerical model uses the 4th order Runge-Kutta scheme to advance in time and has the option of 2nd or 4th order Arakawa Jacobian technique to approximate the advection terms. It has multiple movable or adaptive nests within the base grid. In this study, most of the simulations are run on a base domain of size 4096 km $\times$ 4096 km with 128 $\times$ 128 grid points. There are 4 subsequent nests within the base domain, each of which has half the domain size and mesh size of its mother domain, so that the finest resolution is 2 km. In a few runs, the resolution was increased to 256 $\times$ 256 grid points for the base domain and all the nests.

3 Ring Evolution

Representative examples of the evolution of thin (12 km), wide (60 km), and very wide rings (108 km) are shown in Figs. 2–4. The rotational timescale $\tau = 2\pi r_2/v(r_2)$ for these three rings is about 2 hr.

Thin rings ($r_3 - r_1 \leq 20$ km, Fig. 2) initially break up into many vortices (≥ 6) that rapidly merge into several vortices (4-5) as they rotate around. The resultant vortices persist for tens of rotational timescales before subsequent merger takes place. Such a configuration can be referred to as 'mesovortex' or 'vortex crystal' stage. Thin rings eventually evolve into monopoles.

For wide rings (24 km $\leq r_3 - r_1 \leq$ 104 km, Fig. 3), initial instability takes longer to grow and shows lower wavenumbers. The few (2-5) resulting vortices gradually relax to a monopole.

Very wide rings ($r_3 - r_1 \geq 108$ km, Fig. 4) show wavenumber two structures initially, but they never break up into individual vortices. The central low vorticity remains until the last timestep, which corresponds to about 80 rotational timescales.

4 Initial Wavenumber

Simulation results show that the initial instability wavenumber tends to decrease with increasing ring thickness (Fig. 5). For thin rings ($r_3 - r_1 \leq 20$ km), this decrease is very sharp. For wide rings, there is usually a thickness range that corresponds to the same wavenumber, and the range appears to increase with decreasing wavenumber.

Schubert *et al.* (1999) performed a linear stability analysis for annular rings with piecewise constant radial profiles. Their Fig. 2 shows the unstable regions for wavenumbers 3–8 in $\delta - \gamma$ space, where δ is the ratio of the inner and outer radii and γ is the ratio of the inner vorticity and average vorticity. For the rings I study, $\gamma = 0$. Converting into this notation, the initial wavenumber of my simulations agrees well with Schubert *et al.*'s linear stability results (Fig. 6).

5 Enstrophy History

The evolution of different rings is studied by plotting the normalized enstrophy as a function of time (Fig. 7). For thin rings ($r_3 - r_1 \leq 20$ km), the rapid merger of initial vortices results in a sharp decrease of enstrophy early in the evolution. The enstrophy levels off with time during each mesovortex stage. Each subsequent merger leads to a rapid decrease of enstrophy and thus a stairstep pattern in the enstrophy history.

For wide rings (24 km $\leq r_3 - r_1 \leq$ 104 km), the early stage enstrophy decreases more slowly, consistent with the slower growth of initial instability. Subsequent relaxation to a monopole is gradual, without the transitional mesovortex stage. For very wide rings ($r_3 - r_1 \geq 108$ km), consistent with the central low vorticity remaining unmixed during the entire simulation, the slope of the enstrophy curve does not change much with time.

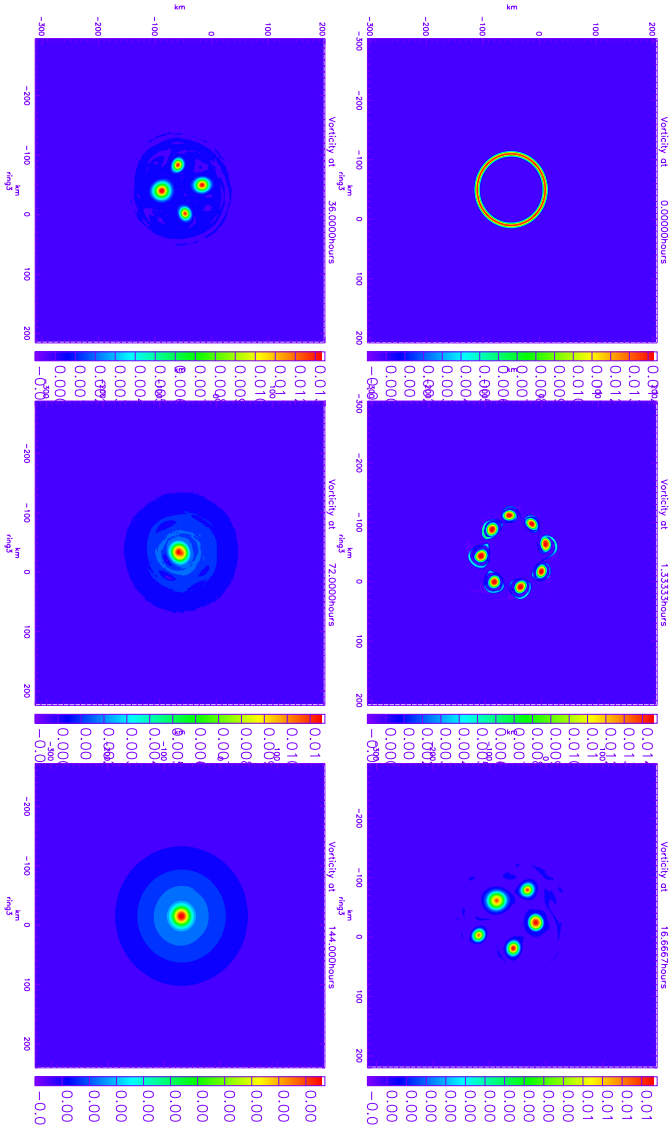

Figure 2: Evolution of thin ring: $r_3 - r_1 = 12$ km.

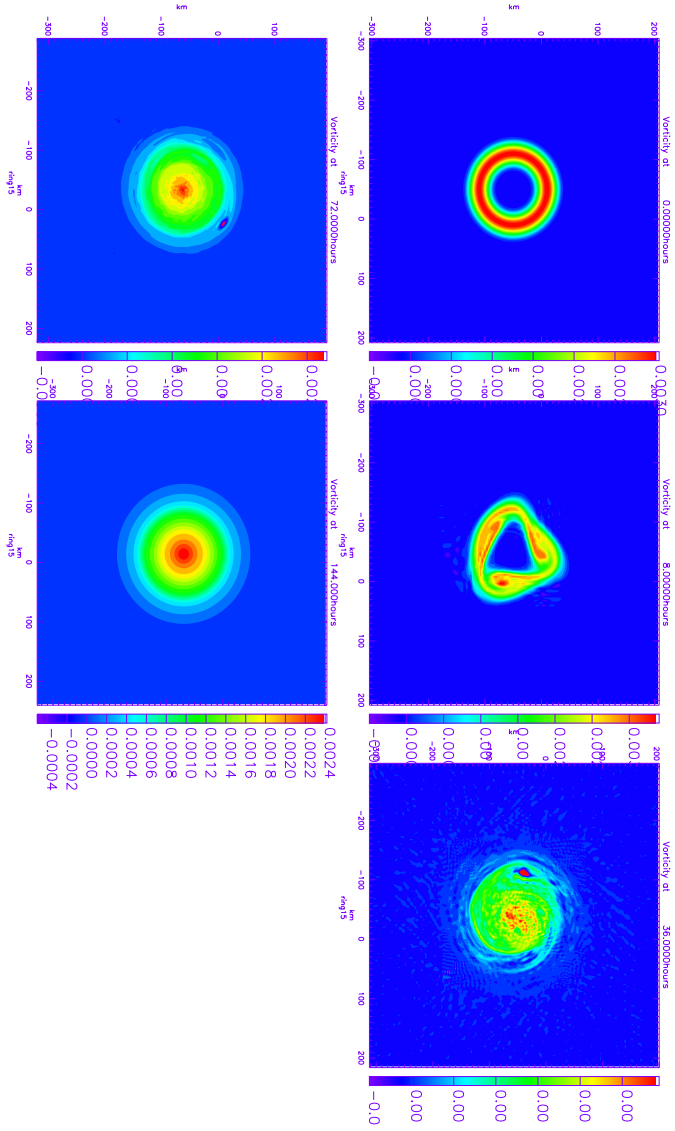

Figure 3: Evolution of wide ring: $r_3 - r_1 = 60$ km.

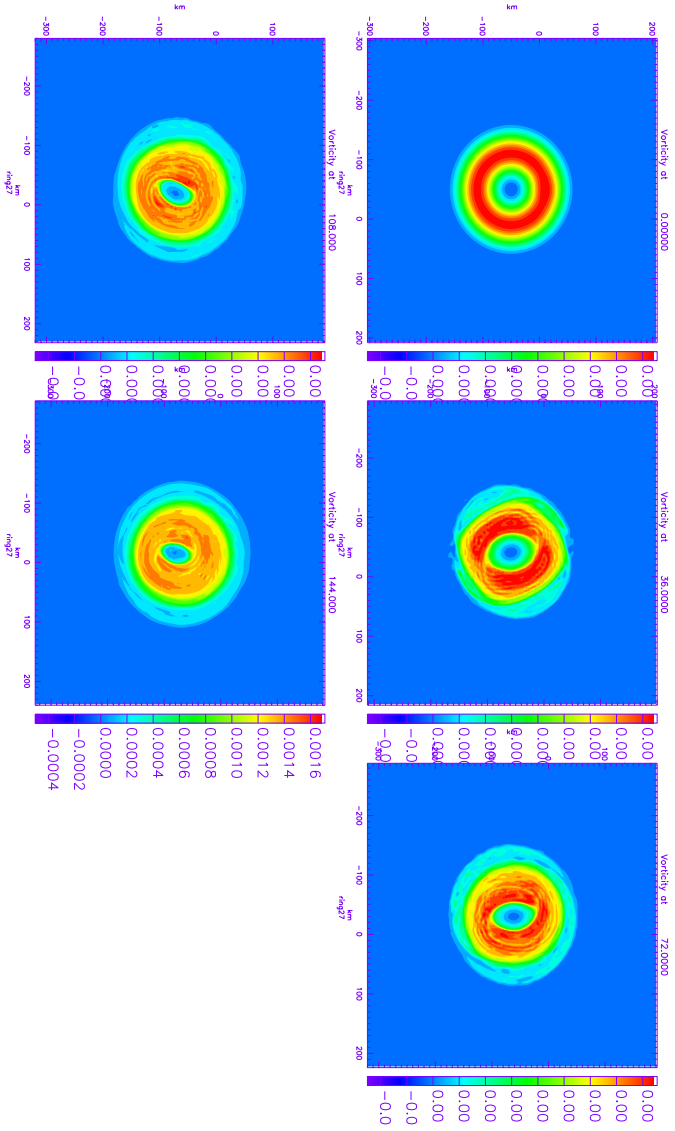

Figure 4: Evolution of very wide ring: $r_3 - r_1 = 108$ km.

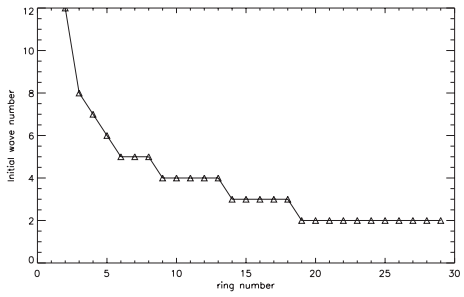

Figure 5: Initial wavenumber as a function of ring number. Ring width = ring number × 4 km.

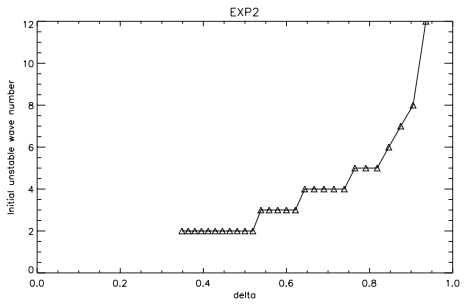

Figure 6: Initial wave number as a function of δ with $\gamma = 0$ for comparison with the linear stability analysis of Schubert *et al.* (1999).

6 The Minimum Enstrophy Theory and Final State

6.1 The Minimum Enstrophy Theory

Consistent with Eq. (6), simulations show that the enstrophy decays much faster than the energy for small diffusivity ν. Based on this result, a minimum enstrophy theory has been applied to predict the final states for annular rings (Schubert *et al.* 1999). The idea is to maximize the enstrophy deficit, i.e. to minimize the final enstrophy, under the constraint of constant energy or angular momentum.

In the case of minimum enstrophy with constrained energy and circulation, I vary the mixing radius b and the wind profile $v(r)$ in the variational problem

$$\begin{aligned} 0 &= \delta \int_0^b \left[\zeta_0^2 - \zeta^2 - \mu^2(v_0^2 - v^2)\right] r dr \\ &= 2\int_0^b \left(-\zeta\delta\zeta + \mu^2 v\delta v\right) r dr + \left[\zeta_0^2(b) - \zeta^2(b)\right] b\,\delta b \\ &= 2\int_0^b \left(\frac{d\zeta}{dr} + \mu^2 v\right) \delta v\, r dr - 2b\zeta(b)\delta v(b) + \left[\zeta_0^2(b) - \zeta^2(b)\right] b\,\delta b \\ &= 2\int_0^b \left(\frac{d\zeta}{dr} + \mu^2 v\right) \delta v\, r dr + \left[\zeta_0(b) - \zeta(b)\right]^2 b\,\delta b \end{aligned} \tag{8}$$

where μ^2 is the Lagrange multiplier, $v_0(r)$ and $\zeta_0(r)$ are the initial wind and vorticity

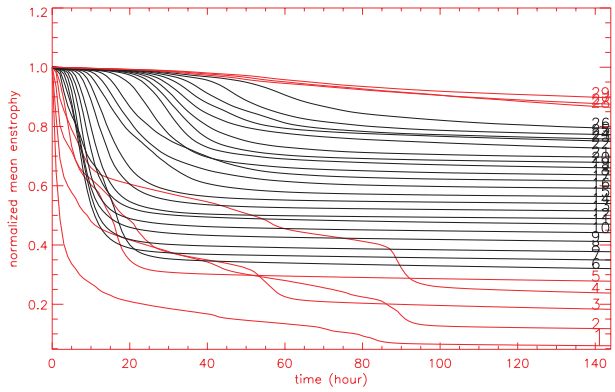

Figure 7: Simulated enstrophy normalized by initial enstrophy as a function of time for the set of rings.

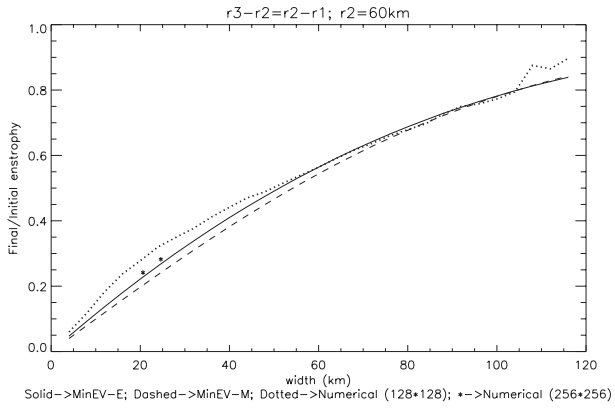

Figure 8: Comparison of theoretical and numerical values of the final enstrophy. Solid line is the prediction of a minimum enstrophy theory with constrained energy. Dashed line is the prediction of a minimum enstrophy theory with constrained angular momentum. Dotted line is the numerical result for runs with 128×128 resolution. Stars are the numerical results for runs with 256×256 resolution.

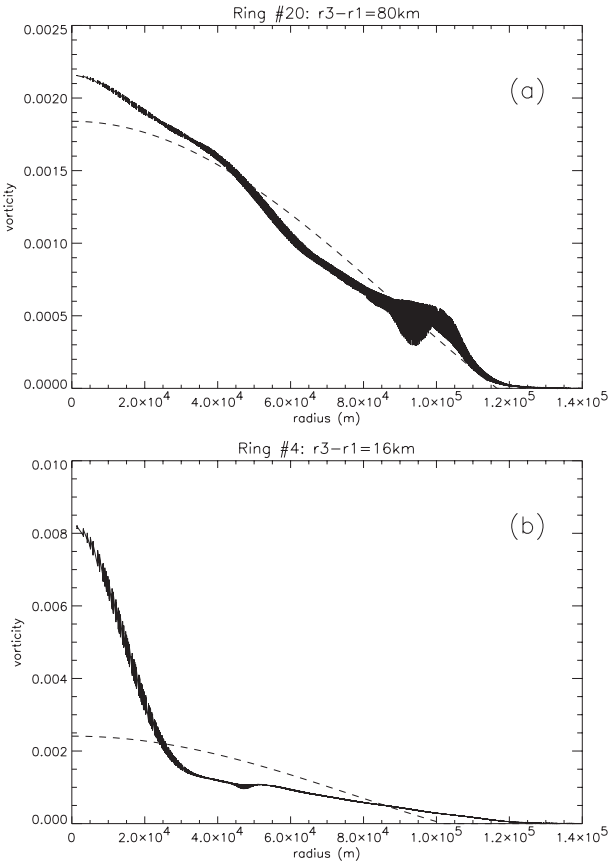

Figure 9: Theoretical and numerical final radial vorticity profile comparison. Numerical results are plotted as scatter plots, Predictions of the minimum enstrophy theory with constrained energy are plotted in dashed lines.

profiles, $v(r) = v_0(r) for r \geq b$. Upon solving the Euler-Lagrange equation resulting from the first term, I obtain the final wind and vorticity profiles

$$v(r) = \begin{cases} v_0(b) J_1(\mu r)/J_1(\mu b) & \text{if } 0 \leq r \leq b \ , \\ v_0(r) & \text{if } b \leq r < \infty. \end{cases} \tag{9}$$

$$\zeta(r) = \begin{cases} v_0(b) \mu J_0(\mu r)/J_1(\mu b) & \text{if } 0 \leq r \leq b, \\ 0 & \text{if } b \leq r < \infty. \end{cases} \tag{10}$$

Requiring $\zeta(b) = \zeta_0(b) = 0$ yields

$$J_0(\mu b) = 0, \tag{11}$$

so that μb must be a zero of the J_0 Bessel function. The first zero yields the lowest enstrophy, so that $\mu b \approx 2.4048$. Substituting Eq. (9) into the energy constraint $\int_0^b v_0^2(r) r dr = \int_0^b v^2(r) r dr$ yields

$$8\pi^2 \int_0^b v_0^2(r)\, r dr = C^2, \tag{12}$$

where $C = 2\pi b v_0(b)$ is the circulation. Given the initial tangential wind $v_0(r)$ and the associated initial vorticity $\zeta_0(r)$, μ, and b can thus be determined from (11) and (12).

Similarly, the final enstrophy can be minimized under the constraint of conservation of angular momentum. This leads to the final wind and vorticity profiles

$$v(r) = \begin{cases} v_0(a)(r/a)[2 - (r/a)^2], & \text{if } 0 \leq r \leq a \ , \\ v_0(r), & \text{if } a \leq r < \infty, \end{cases} \tag{13}$$

$$\zeta(r) = \begin{cases} [4 v_0(a)/a][1 - (r/a)^2], & \text{if } 0 \leq r \leq a, \\ 0, & \text{if } a \leq r < \infty. \end{cases} \tag{14}$$

6.2 Final Enstrophy Comparison

Integrating the square of the predicted final vorticity profile Eq. (10) and the square of the initial vorticity profile Eq. (1), I obtained the final and initial enstrophy for each ring. Comparing the ratio between the final and initial enstrophy with the enstrophy ratio between the last and first time step of the simulation (Fig. 8), I find that the predicted final enstrophy agrees well with numerical results for wide rings. The deviation for very wide rings is related to the persistence of the central low vorticity in the simulation and the relaxation to monopole predicted by theory. The deviation for thin rings can be greatly improved by running the model at higher resolution, as shown by the stars in Fig. 8. A high-resolution simulation is expected to produce a larger differences for thin rings because more grid points are needed to resolve the initial vorticity profiles properly. So, the minimum enstrophy theory is able to predict the final enstrophy of both the thin and the wide rings in my study.

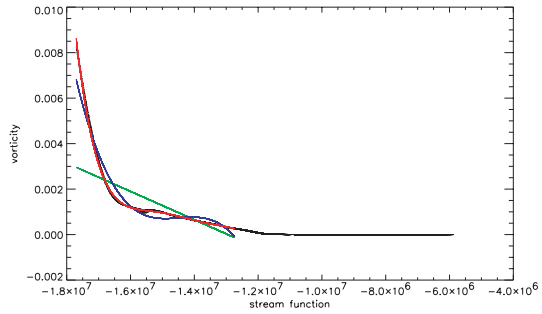

Figure 10: Final vorticity as a function of stream function for thin ring ($r_3 - r_1 = 16$ km). Black line is scatter plot from the final time step. Green line is the prediction of the minimum enstrophy theory with constrained energy. Blue line is a 3rd order polynomial fit for the black scatter plot. Red line is a 5th order polynomial fit for the black scatter plot.

6.3 Final Vorticity Profile Comparison

For wide rings, the vorticity profile predicted by theory, as expressed in Eq. (10) captures most of the features of the simulated final vorticity profile (Fig. 9a). However, for thin rings, the simulated final vorticity considerably overshoots the theoretical prediction at small radii (Fig. 9b). This deviation for thin rings can be viewed in the stream function-vorticity perspective, as shown in Fig. 10. The numerical curve is a scatter plot produced from the vorticity and stream function at every grid point in the output domain at the last time step. Such scatter plots at early times show many fat bands that collapse onto each other with time and eventually become the thin line in Fig. 10. Solving the stream function from (5) with the boundary condition that the final stream function matches the initial stream function at the mixing radius b, I obtain the green line in Fig. 10. This linear relationship is expected from a slight modification of the argument given in (8). If, when proceeding from the second line in (8), we integrate the $v\delta v$ term by parts instead of the $\zeta\delta\zeta$ term, we obtain

$$0 = 2\int_0^b \left(-\zeta - \mu^2\psi\right)\delta\zeta\, r dr + 2\mu^2 b\psi(b)\delta v(b) + \left[\zeta_0^2(b) - \zeta^2(b)\right] b\delta b, \tag{15}$$

so that $\zeta = -\mu^2\psi$ for $0 \le r \le b$. Minimum enstrophy theory approximates the numerical curve by a line, though this curve can be better fit by a 5th order polynomial. This suggests the possible existence of a better variational principle, but I will not pursue this further here.

7 Comparison with Skewed Rings

Two sets of experiments with skewed initial vorticity profiles have been performed to compare with the symmetric rings investigated before. One set has a sharper inner edge, while the other has a sharper outer edge. Sample initial conditions are shown in Fig. 11. All the rings have fixed $r_2 = 60$ km and fixed circulation, as before. The evolution of the enstrophy for the thin and wide rings of the three sets of rings is similar, and the final enstrophy can

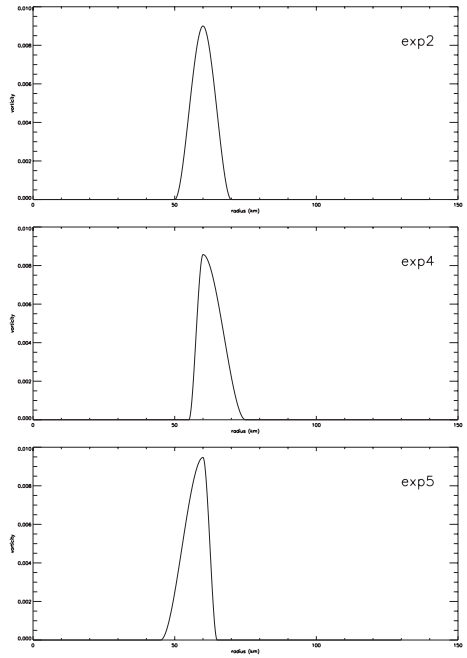

Figure 11: Example initial vorticity profiles for three sets of rings. Exp2: symmetric rings; Exp4: rings with sharper inner edge; Exp5: rings with sharper outer edge.

be predicted by the minimum enstrophy theory. Rings with a sharper inner edge usually have higher initial wave numbers than the others (Fig. 12), and even the widest such ring collapses into a monopole.

8 Conclusion

I have investigated the rearrangement of annular rings of high vorticity in this study. Thin rings initially break up into many vortices that subsequently merge. They often come into a configuration where several vortices rotate around for many rational timescales. Such "mesovortex states" correspond to the "stairs" in the enstrophy history plot. Wide rings have lower initial wavenumbers that take longer to grow, and they gradually evolve into monopoles. Very wide rings usually have low central vorticity throughout the simulation. However, all the rings with sharper inner edges evolve into monopoles. The minimum enstrophy theory is useful for predicting the final enstrophy for both thin and wide rings. Although it does an adequate job of predicting the final vorticity profile for wide rings, it fails for thin rings. Skewed rings with sharper inner edges usually have higher initial wave numbers than other rings with the same width, and this might be predicted by a more sophisticated linear theory than that of Schubert *et al.*

Acknowledgements I would like to thank Wayne Schubert for suggesting this project and guiding me through the summer, Ricardo Prieto for providing the numerical code, and Phil Morrison for help and advice.

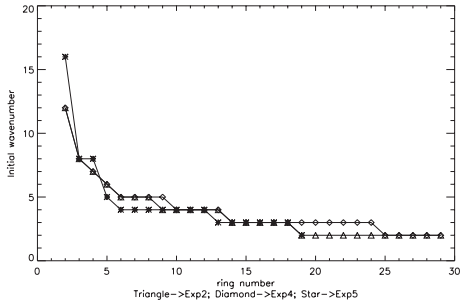

Figure 12: Initial wavenumber as a function of ring number for three sets of rings. $\triangle$ Exp2 symmetric rings, $\diamond$ Exp4 rings with sharper inner edge, $*$ Exp5 rings with sharper outer edge.

References

Fulton, S. R., 2001: An adaptive multigrid barotropic tropical cyclone track model. *Mon. Wea. Rev.*, **129**, 138–151.

Kossin, J. P., and W. H. Schubert, 2001: Mesovortices, polygonal flow patterns, and rapid pressure falls in hurricane-like vortices. *J. Atmos. Sci.*, **58**, 2196–2209.

Schubert, W. H., M. T. Montgomery, R. K. Taft, T. A. Guinn, S. R. Fulton, J. P. Kossin, and J. P. Edwards, 1999: Polygonal eyewalls, asymmetric eye contraction, and potential vorticity mixing in hurricanes. *J. Atmos. Sci.*, **56**, 1197–1223.